Laminar, cellular, transverse, and multiheaded pulsating detonations in condensed phase energetic materials from molecular dynamics simulations

Vasily V. Zhakhovsky,[1,*] Mikalai M. Budzevich,[1] Aaron C. Landerville,[1] Ivan I. Oleynik,[1,†] and Carter T. White[2,‡]
[1]*University of South Florida, 4202 East Fowler Avenue, Tampa, Florida 33620-5700, USA*
[2]*Naval Research Laboratory, Washington DC 20375-5320, USA*
(Received 2 August 2013; published 24 September 2014)

The development of condensed-phase detonation instabilities is simulated using moving window molecular dynamics and a generic AB model of a high explosive. It is found that an initially planar detonation front with one-dimensional flow can become unstable through development of transverse perturbations resulting in highly inhomogeneous and complex two- and three-dimensional distributions of pressure and other variables within the detonation front. Chemical reactions are initiated in localized transverse shock fronts and Mach stems with a pressure and temperature higher than those predicted by classic Zel'dovich, von Neumann, and Doering detonation theory. The two-dimensional cellular and transverse and three-dimensional pulsating detonation structures are found by varying the physico-chemical properties of AB energetic material, sample geometry, and boundary conditions. The different regimes of condensed-phase detonation that can develop from instabilities within a planar detonation front exhibit structures, although at a much smaller scale, that are similar to those observed in gases and diluted liquids.

DOI: 10.1103/PhysRevE.90.033312 PACS number(s): 02.70.Ns, 47.40.Rs, 62.50.Ef, 82.40.Fp

I. INTRODUCTION

Detonation is a shock-induced reaction wave propagating at supersonic speeds within an energetic material (EM) [1,2]. Owing to their practical importance, detonation physics and chemistry have been the focus of intensive experimental and theoretical investigations for more than a century [1,2]. Chapman [3] and Jouguet [4,5] (CJ) were the first to develop a hydrodynamic theory of detonation, which was based on the assumption of an infinitesimally thin reaction zone. In the 1940s, Zel'dovich [6], von Neumann [7], and Doering [8] (ZND) made an important step forward by considering more complex structures of the detonation front, including the leading shock wave, which compresses and heats the unreactive material, followed by an extended reaction zone, in which the EM is transformed into the reaction products accompanied by a drop in pressure [1,2,9].

ZND theory, being intrinsically one-dimensional (1D) (the detonation front is considered to be planar) [1,2,9], was successful in predicting average detonation speeds and physical properties at the CJ point in good agreement with experiment. However, numerous experimental [10–16] and theoretical [17–25] investigations of detonations in gases have demonstrated that the detonation front can be much more complex, exhibiting two-dimensional (2D) cellular and three-dimensional (3D) pulsating-turbulent detonation structures. The chemical reactions behind these nonplanar shocks are initiated in local high-pressure spots having compressions and temperatures higher than those in the von Neumann spike of 1D ZND theory [2]. Pulsating-turbulent detonations were also observed in diluted liquid EMs [16,26,27].

In contrast to gases, complex 2D or 3D detonation structures have not been observed yet in the condensed phase (with the exception of diluted liquids [1,27]). The processes within condensed-phase detonation fronts occur at much shorter time and length scales that, when combined with the violent nature of explosions, make experimental observation of the detonation microstructure difficult, if not impossible. However, such short time and length scales are accessible to molecular dynamics (MD) simulations, thus providing an excellent opportunity for detailed investigation of complex detonations in the condensed phase.

MD simulations of detonations require atomistic potentials that are capable of simultaneously following the dynamics of a large number of atoms in a rapidly changing environment while including the possibility of exothermic chemical reactions. The reactions should also proceed along chemically reasonable reaction paths from the cold solid-state reactants to the hot gas-phase molecular products. For molecular solids that are typical of energetic materials, these potentials must incorporate both the strong intramolecular forces that bind atoms into molecules and the weak intermolecular forces that bind molecules into solids.

In the late 1980s and early 1990s, reactive empirical bond order (REBO) potentials with these essential ingredients were introduced and refined to describe perhaps the simplest generic model of a high explosive: a molecular solid made up of diatomic AB molecules that when shocked could undergo exothermic chemical reactions to form more stable A_2 and B_2 molecular products [28–31]. The half reactions $A + AB \rightarrow A_2 + B$ and $B + BA \rightarrow B_2 + A$ that drive the detonation in this model each liberate 3 eV of energy similar to the exothermic reaction $N + NO \rightarrow N_2 + O + 3.3$ eV [32] thought important in the detonation of solid nitric oxide. The AB model and its refinements allowed for atomic-scale simulation of the entire process of self-supported materials detonation yielding results consistent with continuum ZND theory [30,33], including a well-defined von Neumann spike, sonic point, steady flow from the leading shock front to the sonic point, and a detonation speed determined directly from the MD simulation within less than 1% of that calculated from continuum theory using the CJ condition [31].

*6asi1z@gmail.com
†oleynik@usf.edu
‡carter.white@nrl.navy.mil

More recently Heim *et al.* found that a version of the AB model could support a cellular detonation structure in 2D samples [34]. Their results suggest that even the minimalist AB model, suitably parameterized, can capture complex detonation behavior. However, all simulations to date employing the AB model required an ever increasing number of atoms to follow the detonation as it propagates through the solid. This coupling of time and length scales is a serious stumbling block for further advances in MD simulations of detonation due to the requirements of longer times and larger samples.

We avoid this stumbling block by using a moving window molecular dynamics (MW-MD) technique [35,36] that allows an AB detonation to be simulated for an indefinite period of time. MW-MD has already been used to uncover a hitherto neglected two-zone regime of shock wave propagation that should be considered in any study of shock-induced plasticity in solids [36]. It has also been used to bring results from MD simulations into agreement with experiment by following the evolution of shock-induced orientation-dependent metastable states towards an orientation-independent final state Hugoniot in face-centered-cubic (fcc) metals [37].

Herein we use MW-MD to reveal instabilities that could develop in a planar detonation front propagating in an EM described by the AB model. Consistent with earlier results, we find that the model can support a steady 1D planar detonation. However, by varying physico-chemical properties of the AB EM, sample geometry, and boundary conditions, we find instabilities that can later develop into steadily propagating but complex 2D and 3D detonations.

In the next section we show how the AB model is modified to allow the reaction barrier to be easily changed while preserving its realistic properties. Then in Sec. III we describe how ZND theory applied to this model is used to obtain starting input for our large-scale MW-MD calculations. In Sec. IV we outline the MW-MD method itself and explain its use in detonation simulations. In Sec. V we present a series of MW-MD results that illustrate how instabilities within an initially 1D detonation in the AB model can evolve into 2D cellular, 2D transverse, and 3D pulsating-turbulent detonation structures that reflect those reported in the gas phase [10–16,26,27]. Finally, a summary and concluding remarks are provided in Sec. VI.

II. MODIFIED AB REBO POTENTIAL

In the original AB model,[31] the binding energy of N atoms is given by

$$U = \sum_{i,j>i}^{N} \{f_c(r_{ij})[V_R(r_{ij}) - \overline{B}_{ij} V_A(r_{ij})] + V_{vdW}(r_{ij})\}. \quad (1)$$

The pairwise repulsive,

$$V_R(r_{ij}) = \frac{D_e}{S-1} \exp\{[-\alpha\sqrt{2S}(r_{ij} - r_e)]\}, \quad (2)$$

and attractive,

$$V_A(r_{ij}) = \frac{SD_e}{S-1} \exp\{[-\alpha\sqrt{2/S}(r_{ij} - r_e)]\}, \quad (3)$$

interactions are combined in (1) using the bond order $\bar{B}_{ij} = (B_{ij} + B_{ji})/2$,

$$B_{ij} = \left\{1 + G \sum_{k\neq i,j} f_c(r_{ik}) \exp[m(r_{ij} - r_{ik})]\right\}^{-n}, \quad (4)$$

to produce short-range potentials describing covalent interactions between atoms i and j that are cut off by $f_c(r_{ij})$ when the separation r_{ij} between these atoms is large.

The bond order $\bar{B}_{ij}$ in Eq. (1) introduces many-body effects into the potential by modifying $V_A(r_{ij})$ according to the local environment. These many-body effects arise from electronic degrees of freedom, which are not explicitly included in the model. For an isolated diatomic molecule, $\bar{B}_{ij} = 1$ so that the potential $[V_R(r_{ij}) - \bar{B}_{ij} V_A(r_{ij})]$ reduces to a generalized Morse function of the type used to describe diatomic bonding with bond length r_e, well depth D_e, and force constant $2\alpha^2 D_e$. For more coordinated structures, $\bar{B}_{ij}$ decreases with increasing number of competing bonds available to atoms i and j, thus reflecting the finite number of valence electrons that these atoms have available for bonding. When the coupling G in Eq. (4) is small, the strength of a given bond is not strongly reduced by competing bonds, and the potential will favor highly coordinated metallic systems. At the other extreme, when G is large, the potential favors a few strong bonds such as those in molecular solids.

By introducing two types of atoms A and B of equal concentrations and choosing $S = 1.8$, $r_e = 0.1$ nm, $\alpha = 27$ nm^{-1}, $m = 22.5$ nm^{-1}, $n = 0.5$, $\text{mass}_{\text{A,B}} = 14$ amu, $D_e^{AB} = 2$ eV $= 192.9738$ kJ/mol, and $D_e^{AA} = D_e^{BB} = 5$ eV, Eq. (1) can be used to describe AB molecules bound together into a molecular solid by a weak long-range van der Waals potential $V_{vdW}(r_{ij})$. When shocked, the diatomic AB molecules making up this solid can undergo exothermic chemical reactions along chemically reasonable pathways to more stable A_2 and B_2 molecular products, leading to a chemically sustained shock wave with properties consistent with the classic ZND continuum theory of detonations. Herein we employ a modified version of the AB model that speeds up the evaluation of the potential while allowing the reaction barrier to be easily adjusted without sacrificing the essential features of the model.

First, $f_c(r_{ij})$ in the original AB model is replaced by

$$f_c(r_{ij}) = \begin{cases} \dfrac{\left(1 - \frac{r_{ij}}{r_m}\right)^2}{\left(1 - \frac{r_{ij}}{r_m}\right)^2 + a_c \left(\frac{r_{ij}}{r_m}\right)^{12}}, & r_{ij} \leqslant r_m \\ 0 & r_{ij} > r_m, \end{cases} \quad (5)$$

where $a_c = 0.75$ and $r_m = 0.24$ nm. Second, the long-range van der Waals interaction $V_{vdW}(r_{ij})$ in (1) is now represented by a customized Lennard-Jones potential [38]

$$V_{\text{LJ}}(r_{ij}) = 4\epsilon[(\sigma/r_{ij})^{12} - (\sigma/r_{ij})^6] - c_2\left(r_{ij}^2 - r_0^2\right) - c_3(r_{ij} - r_0)^3 \quad (6)$$

smoothly switched to zero at $r_{\text{LJ}} = 0.469$ nm by requiring that c_2 and c_3 are such that $V_{\text{LJ}}(r_{\text{LJ}})$ and $V'_{\text{LJ}}(r_{\text{LJ}})$ both vanish, where

the LJ parameters $\epsilon = 5 \times 10^{-3}$ eV and $\sigma = 0.2988$ nm were taken as in Ref. [31] so that the position of the LJ minimum $r_0 = \sqrt[6]{2}\sigma$ is given by $r_0 = 0.3354$ nm. Then, following Heim *et al.* [39], rather than interpolating $V_{\mathrm{LJ}}(r_{ij})$ directly to zero within the bonding region, it is now monotonically interpolated from $r_p = 0.3$ nm inward to a constant, positive plateau ϵa_0 applied for $r_{ij} \leqslant r_s$, using the polynomial function $p(r)$,

$$p(r_{ij}) = \epsilon[a_0 + (r_{ij} - r_s)^3(a_3 + a_4(r_{ij} - r_s) + a_5(r_{ij} - r_s)^2)], \quad (7)$$

where the constants a_3, a_4, and a_5 are determined by requiring that $p(r_p) = V_{\mathrm{LJ}}(r_p)$, $p'(r_p) = V'_{\mathrm{LJ}}(r_p)$, and $p''(r_p) = V''_{\mathrm{LJ}}(r_p)$. These conditions ensure that $p(r_{ij})$ not only smoothly joins the plateau ϵa_0 at r_s, but also the LJ potential $V_{\mathrm{LJ}}(r_{ij})$ at r_p. Finally, D_e in Eq. (2) and Eq. (3) are shifted downward by an amount equal to ϵa_0 to compensate for the plateau, thus arriving at the same well depth and diatomic bond distance specified in the original model. At this point all parameters, either input or derived, of the AB model used herein are specified once values of a_0 and r_s are assumed.

Taken together, the changes to the AB model described in the previous paragraph leave intact the chemical and van der Waals binding energies of the original model [31], while allowing the physico-chemical properties of the AB model to be varied by adjusting just one parameter, a_0. Specifically, the height of the plateau ϵa_0 influences both the equation of state (EOS) and the reaction barrier E_b for the half reactions $\mathrm{A} + \mathrm{AB} \rightarrow \mathrm{A_2} + \mathrm{B} + 3\,\mathrm{eV}$ and $\mathrm{B} + \mathrm{BA} \rightarrow \mathrm{B_2} + \mathrm{A} + 3\,\mathrm{eV}$, which drive the detonation. Furthermore, these adjustments are accomplished while maintaining chemically reasonable potential energy surfaces for the generic half reactions with the transition state occurring along the minimum energy pathway in a collinear geometry with an early barrier typical of atom-diatom reactions. As an example, the potential energy surface for the reaction $\mathrm{A} + \mathrm{AB} \rightarrow \mathrm{A_2} + \mathrm{B} + 3$ eV, with $E_b = 0.367$ eV, shown in Fig. 1 is obtained by taking $a_0 = 50$ and $r_s = 0.2$ nm.

The variations of both thermophysical properties and reactive chemistry of the AB model produce markedly different detonation behaviors. Different cases are labeled in this work using the reaction barrier E_b. Although E_b increases with increasing a_0, it has to be determined numerically by searching for the transition state once a_0 and r_s are specified. Increasing a_0 and hence E_b also steepens the isotherms of the products resulting in an upward shift of the CJ point, thus causing an increase in pressure and speed of the self-sustained detonation. See Fig. 2 and Sec. III. In this work, four reaction barriers, $E_b = 0.367$, 0.245, 0.198, and 0.101 eV, are used. The first three values of E_b result from taking $r_s = 0.2$ nm, with $a_0 = 50.0$, 28.448, and 20.0, respectively, while the last one results from taking $r_s = r_m = 0.24$ nm, with $a_0 = 2.85$.

III. AB MODEL DETONATION PROPERTIES FROM 1D ZND THEORY

We first apply ZND theory to the current AB model to obtain an estimate for the detonation speed D_{CJ}, which is used as an input parameter to start the large-scale MW-MD simulations.

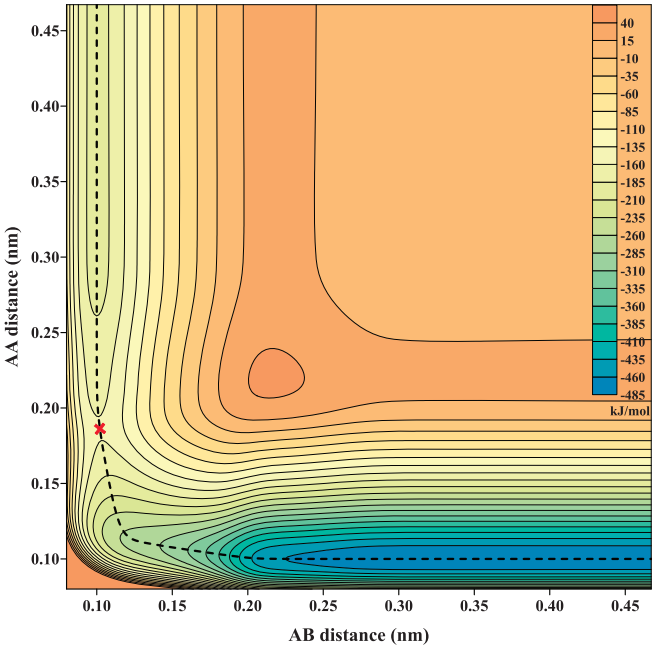

FIG. 1. (Color online) 2D map of potential energy for linear three-atom system AAB. The dashed line shows the reaction pathway $\mathrm{A} + \mathrm{AB} \rightarrow \mathrm{A_2} + \mathrm{B}$. The X on the reaction pathway is the position of the transition state.

For complex 2D and 3D detonations the true detonation speed determined from MW-MD turns out to be somewhat different from that predicted by 1D ZND theory. Nevertheless, D_{CJ} is close enough to the actual detonation speed to accelerate convergence of the MW-MD calculations to the true detonation speed.

ZND theory, as usually sketched, views a detonation as starting with a rapid compression and heating caused by the leading shock wave, which causes reactions to begin which then proceed, accompanied by a drop in pressure, within

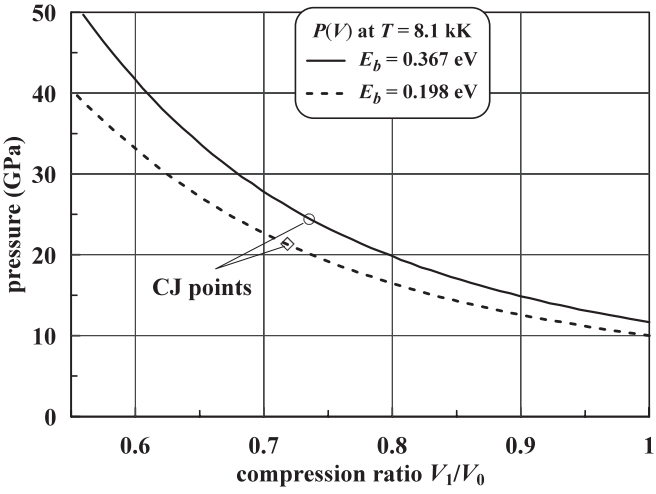

FIG. 2. Product isotherms from the AB model with different reaction barriers E_b. Diamonds indicate the positions of the CJ points calculated in Sec. III. These hot materials are made from products of combustion of AB molecules (mainly AA and BB molecules).

the reaction zone. This rapid initial compression followed by slower chemistry produces a pressure peak, known as the von Neumann spike, near the leading edge of the detonation front. Next, ZND theory assumes that the flow, starting at the leading edge of the shock front and extending throughout the reaction zone, although certainly not in chemical equilibrium everywhere, is nevertheless steady. This is the simplest assumption consistent with the requirement that the reaction zone must keep pace with the shock front to sustain the detonation at net constant speed. ZND theory also assumes that the flow is not only steady, but also in equilibrium by the time it reaches the end of the reaction zone well behind the leading shock front. Finally, it assumes that the detonation moves with the minimum speed $D_{\rm CJ}$, consistent with the assumption of steady flow. This last constraint is known as the CJ condition, which was put on a firmer foundation by Zel'dovich [6,9].

The problem, then, is to combine the above conditions to extract $D_{\rm CJ}$. This is done by first recalling that the conservation of mass, momentum, and energy, when combined with the assumption of a steady flow reaching equilibrium at the end of the reaction zone, require

$$P_1 = P_0 + \left(\frac{D}{V_0}\right)^2 (V_0 - V_1) \tag{8}$$

and

$$\epsilon_1(P_1,V_1) - \epsilon_0(P_0,V_0) = \tfrac{1}{2}(P_0 + P_1)(V_0 - V_1) \tag{9}$$

for a detonation moving with speed D. These equations relate the undisturbed explosive lying at rest with pressure $P_0 = 0$, specific volume $V_0 = 1/\rho_0$, and specific internal energy ϵ_0, to the state at the end of the reaction zone with pressure P_1, specific volume $V_1 = 1/\rho_1$, and specific internal energy ϵ_1. Equation (8) is for a straight line with a slope proportional to D^2. This line, known as the Rayleigh line, connects the initial state preceding the detonation to the final state at the end of the reaction zone.

The detonation Hugoniot (also known as the Crussard curve) is given by the set of points $\{P_1, V_1\}$ satisfying Eq. (9) assuming that P_0 and V_0 are known. Because Eq. (9) does not involve D, the detonation Hugoniot can be represented as a function of the form $P_1 = H(V_1; P_0, V_0)$. Once $H(V_1; P_0, V_0)$ is determined, then Eq. (8) and the CJ condition can be used to determine $D_{\rm CJ}$.

To calculate the detonation Hugoniot, equal numbers of AA and BB molecules were first placed within a box at a density $\rho_0 = 1/V_0$ corresponding to the unshocked solid. The box size was then adjusted to yield a given specific volume V_1. Next, with periodic boundary conditions (PBCs) enforced at all box edges, constant number of particles, volume, and temperature (NVT) MD simulations were performed to bring the system to equilibrium at a specified temperature T_1, chosen within the range 7–10 kK. ϵ_1 and P_1 were then measured from this equilibrium state. This procedure was then repeated for a series of different values of V_1, within the range $0.55V_0 \leqslant V_1 \leqslant V_0$, to obtain a value of P_1 on the isotherm $P_1(V_1; T_1)$, which solves Eq. (9) and hence gives one (V_1, P_1) point of the detonation Hugoniot. The whole process is then repeated for a series of different values of T_1 to obtain the full detonation Hugoniot $P(V)$, as depicted in Fig. 3.

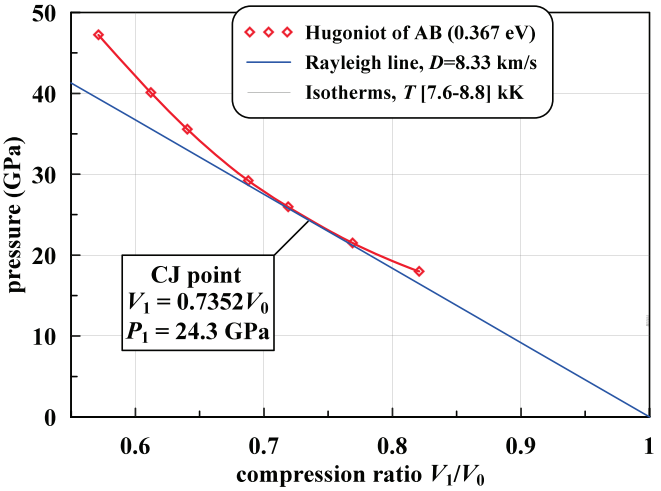

FIG. 3. (Color online) The family of $P_1(V_1)$ isotherms for $E_b = 0.367$ eV. The highlighted line with diamonds is the detonation Hugoniot, the straight solid line is the Rayleigh line just touching the detonation Hugoniot at the CJ point.

For a point on the detonation Hugoniot, if V_1 is specified, then so too is P_1, which allows D, as a function of V_1, to be determined using Eq. (8). The CJ volume $V_{\rm CJ}$ and corresponding CJ pressure $P_{\rm CJ}$ and detonation speed $D_{\rm CJ}$ are then found by choosing the value of V_1 on the detonation Hugoniot that yields the minimum value of $D(V_1)$, as illustrated in Fig. 4. $D_{\rm CJ}$ calculated this way is given by 7.02, 7.55, 8.2, and 8.33 km/s for $E_b = 0.101$, 0.198, 0.245, and 0.367 eV, respectively.

IV. DETONATION SIMULATIONS BY MW-MD

A. MW-MD

Within the MW-MD approach [35,36,38,40], the shock wave structure is simulated in the reference frame moving with the detonation wave. This is achieved by feeding unreacted

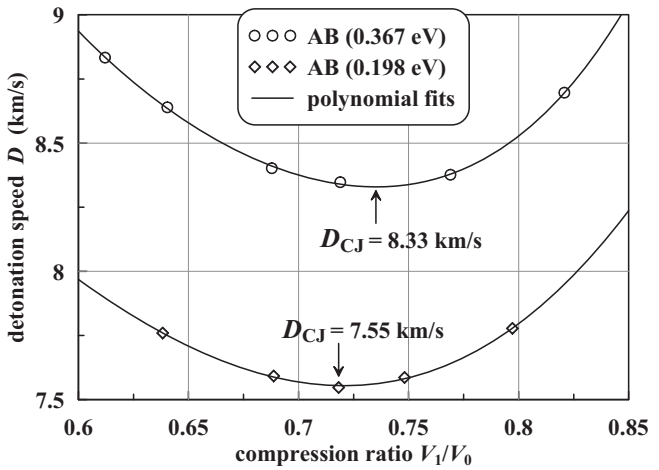

FIG. 4. Detonation speed $D(V_1)$ for two cases corresponding to $E_b = 0.198$ and 0.367 eV. The minimum of $D(V_1)$ at $V_{\rm CJ}$ specifies the CJ point on the detonation Hugoniot.

material into a simulation box upstream from the detonation front, while removing the material from the opposite end of the box downstream from the front. The effective decoupling of time and length scales in MW-MD simulations allows detailed study of the complex processes taking place within the front over a long period of time without having to continually increase the number of atoms in the simulation.

To initiate a compression of the EM and ignite chemical reactions at the beginning of the simulation, a short-range potential barrier of finite height is applied at the left (downstream) boundary. Once the reactions start and a self-sustained detonation begins, the barrier is removed. The removal of the atoms at the left boundary of the simulation cell takes place in the rarefaction tail of the reaction products. This tail moves with supersonic velocity relative to the detonation front and reaction zone. Therefore, once the system has stabilized, any perturbations at the left boundary cannot affect the processes upstream, including the shock front and reaction zone. The ability to control the physico-chemical properties of AB explosive, as well as the geometry of the sample, including its dimensions and boundary conditions in transverse directions within MW-MD simulations, allows for a systematic investigation of various regimes of detonation.

B. Analysis of chemical composition of reactive AB material

To explore the chemical composition of the reactive AB material, fractions of atoms A and B are calculated for reactant AB molecules, and product A_2 and B_2 molecules. To effectively determine whether a pair of atoms i and j constitute a diatomic molecule, the following criteria are applied: (i) atom i is closest to atom j, and atom j is closest to atom i; (ii) the distance between i and j is less than $1.5r_e$; and (iii) the sum of the kinetic energies of i and j in the pair's center of mass reference frame and their potential energies is negative. If any of the above criteria are not satisfied for atoms i and j, then they are termed "radicals." To analyze the chemical composition, the following three fractions are calculated for a selected spatial domain: the product fraction $\lambda(A_2, B_2) = (N_{AA} + N_{BB})/N$, the reactant fraction $\lambda(AB) = N_{AB}/N$, and the radical fraction $\lambda(A^*, B^*) = (N_A + N_B)/N$, where $(N_{AA} + N_{BB})$ is the number of A and B atoms bound in A_2 and B_2 molecules, N_{AB} is the number of A and B atoms bound in AB molecules, $(N_A + N_B)$ is the number of radicals in the domain, and $N = N_A + N_B + N_{AA} + N_{BB} + N_{AB}$ is the total number of atoms within the domain.

C. Starting simulations

The studies of instability development in an initially planar detonation front require a starting 1D detonation. It is prepared by using a sample of small transverse dimensions to produce a stable or quasistable (one that initially persists for some time but is later destroyed by longitudinal perturbations) 1D laminar flow within the sample. The flow in this small sample is begun by assuming the detonation speed predicted by ZND theory as applied to the AB model for a particular E_b, and then allowing this speed to settle to a stable or quasistable value. The upstream unshocked material fed into the MW-MD simulation is obtained by starting from an fcc crystal with the AB molecules oriented along the [100] crystallographic direction and then using a Langevin thermostat in an upstream zone 10 nm thick to relax the structure to a final fcc equilibrium solid with $P = 0$, $T = 40$ K, and unit cell volume of 0.141 nm^3.

The longitudinal direction x corresponds to the direction of propagation for the detonation front, whereas PBCs are imposed in the transverse y and z directions. On occasion, rigid-wall boundary conditions (RBCs), rather than PBCs, are imposed in the transverse directions to study their effect on the detonation wave structure. In almost all simulations the x axis was chosen along the [110] crystallographic direction. Extra simulations were performed for the x axis oriented along the [100] and [111] directions to demonstrate orientation independence of the detonation velocities and CJ points.

Throughout this work a small sample with longitudinal dimension $L_x = 200$ nm and transverse dimensions $L_y = 8.1$ nm and $L_z = 7.8$ nm is used to prepare flow parameters for simulations of samples with larger cross section. This is done by restarting MW-MD simulations with the flow parameters of the smaller sample (atomic coordinates and velocities) replicated in the transverse y and/or z directions. The whole process can be repeated for different values of E_b to investigate the effects of chemistry and thermophysical properties (e.g., EOS) of the AB solid. The use of quasisteady 1D detonation flow as a starting point for investigation of 2D and 3D detonation front instabilities is common in computational fluid dynamics simulations of gas-phase detonations [23].

The versatility of the MW-MD technique allows for systematic study of the evolution of initially planar 1D detonation fronts into more complicated 2D and 3D structures associated with the development of detonation instabilities.

V. PLANAR AND NONPLANAR DETONATION FRONTS

A. 1D laminar detonation

A stable laminar 1D flow with a planar detonation front is observed in our MW-MD simulations using AB crystals with reaction barriers 0.101 and 0.198 eV, and small transverse dimensions $L_y = 8.1$ nm and $L_z = 7.8$ nm, over which PBCs are applied. In both cases a steady unsupported detonation is established after a shock wave is initiated by the piston at the left boundary of the simulation box. The detonation speeds $D = 7.02$ and $D = 7.54$ km/s obtained from our MW-MD simulations for $E_b = 0.101$ and 0.198 eV, respectively, are in excellent agreement with the corresponding speeds $D = 7.0$ and 7.55 km/s predicted from 1D continuum ZND theory (see Sec. III). In both instances, the planar detonation front structure exhibits the major features of a 1D ZND detonation. For the AB model, these include a shock-wave front followed by a von Neumann spike where most of the reactant AB molecules have lost their molecular identity, followed by the reaction zone where A_2 and B_2 molecules are principally formed, and an after-shock laminar flow in chemical equilibrium, all of 1D character. See profiles of various variables in Fig. 5 obtained for the specific case $E_b = 0.198$ eV.

The detonation front thickness is reduced from ~7 to ~5 nm upon increase of E_b from 0.101 to 0.198 eV. When $E_b = 0.198$ eV, small nanometer-sized ripples appear within the 1D detonation front, but the front still remains stable

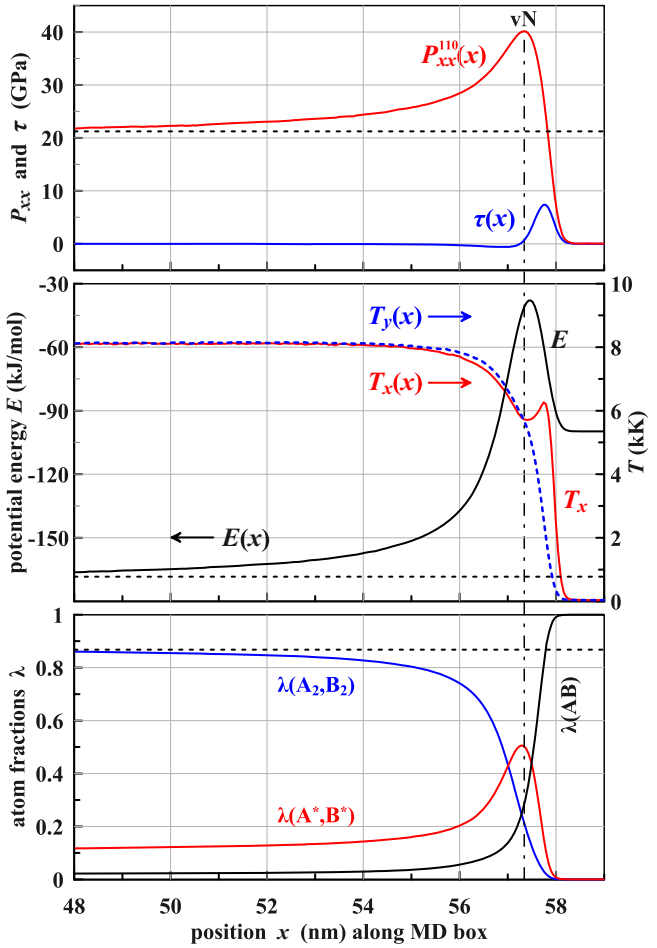

FIG. 5. (Color online) 1D laminar detonation wave structure in AB EM crystal with $E_b = 0.198$ eV. Top panel: Pressure in the direction of detonation propagation $P_{xx}(x)$, and shear stress $\tau(x)$; middle panel: potential energy per atom profiles $E(x)$, and $T_x(x)$ and $T_y(x)$ components of temperature; bottom panel: atom fractions in radicals $\lambda(A^*,B^*)$, products $\lambda(A_2,B_2)$, and reactants $\lambda(AB)$ across the 1D self-sustained detonation wave moving at $D = 7.55$ km/s. The dotted horizontal lines show the corresponding values at the CJ point. The dashed vertical line indicates the position of the von Neumann (vN) spike.

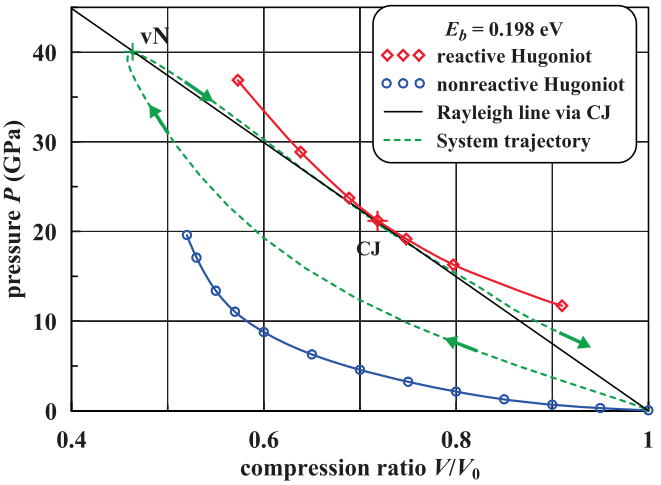

FIG. 6. (Color online) The nonreactive and reactive Hugoniots for $E_b = 0.198$ eV. The nonreactive Hugoniot cannot be extended to the vN point because the system begins to react. Also shown is the Rayleigh line starting at the unshocked state, and determined by the CJ condition. In addition, the system trajectory in P-V space from the unshocked state to the CJ state and beyond is depicted. The pressure P along this trajectory is defined by $P \equiv \frac{1}{3}(P_{xx} + P_{yy} + P_{zz})$. Initially the system trajectory deviates significantly from the Rayleigh line because the transverse and longitudinal components of the pressure are unequal. However, it coincides with the Rayleigh line as the CJ point is approached from above and these components equalize. After the CJ point these pressure components remain equal but the system trajectory again deviates from the Rayleigh line because the flow behind the CJ point is no longer steady.

without further development of ripples. In both cases, the 1D detonation remains stable upon increase of one of the sample's transverse dimensions, from 8 to 105 nm, for at least 1 ns, the maximum time allowed in our simulations. Although simulations with the third dimension extended beyond 16 nm were not undertaken, it is highly unlikely that it would result in the development of instabilities in AB samples with $E_b = 0.101$ and 0.198 eV.

In idealized ZND theory it is often assumed that the explosive follows the Rayleigh line given by Eq. (8) up to the point of maximum compression known as the vN point, and then relaxes down along this line to the CJ point. However, the calculated hydrostatic pressure does not follow this path to the vN point as illustrated by Fig. 6 for $E_b = 0.198$ eV. This behavior arises because anisotropic compression at the front initially leads to unequal longitudinal and transverse components of both the pressure tensor and kinetic temperature. For this case, different pressure components are reflected by the nonzero shear stress in the top panel of Fig. 5, and different kinetic temperature components by the well-known overshoot in T_x at strong shock fronts [35,40–42] seen in the middle panel of Fig. 5. Nevertheless, by the time the simulation reaches the vN point it has had time to largely equalize the components of temperature and pressure, and the system trajectory closely coincides with the Rayleigh line as the CJ point is approached from above, as shown in Fig. 6. A similar picture applies for $E_b = 0.101$ eV.

In idealized ZND theory it is also often assumed that the system reaches the vN point without reacting, $\lambda(AB) = 1$, whereupon reactions are assumed to begin and run to full completion, $\lambda(A_2,B_2) = 1$, as the system moves down along the Rayleigh line to the CJ state. However, we see from the lower panel of Fig. 5 that at the vN point only ~25% of atoms belong to reactants with an equivalent number in products, and the majority not in well-defined diatomic molecules. In fact, near the vN point $\lambda(A^*,B^*)$ peaks because the high pressure and temperature there strongly favor the loss of molecular identity. In the flow behind the vN point most of these atoms gradually condense into products reaching equilibrium reactant, free atom, and product fractions of ~2, ~11, and ~87%, respectively, at the CJ point. Thus, rather than viewing the vN point as separating a leading rapidly compressed unreacted zone from a following reaction zone at the end of which only product molecules exist, it can be viewed in this simulation as approximately separating a

leading dissociative zone, where the majority of reactants loose their molecular identity, from a following associative zone where the majority of products are formed. A similar picture applies for $E_b = 0.101$ eV.

The fact that a majority of reactants are already destroyed by the time the vN point is reached in the simulated laminar detonations is also consistent with our inability to calculate an unreacted Hugoniot, $\lambda(AB) = 1$, that extends to the vN point. See, for example, Fig. 6. For this case, the problem is to obtain a metastable solution to Eq. (9) with $\lambda(AB) = 1$ at a pressure above $P \sim 20$ GPa. However, this requires a temperature greater than 1.48 kK, which causes reactions to rapidly begin.

Although many of the results described in the previous three paragraphs illustrate that ZND theory, as often sketched, is an oversimplification, they do not undermine the fundamental tenets of the theory used to calculate the detonation speed from the detonation Hugoniot. In the simulations both planar detonations are to an excellent approximation steady from the leading edge of the shock front to the sonic (CJ) point, have reached mechanical and chemical equilibrium at that point, and move with the minimum speed consistent with the assumption of steady flow. In ZND theory these are the only requirements needed to determine the detonation speed from the detonation Hugoniot. Indeed, the numbers reported at the beginning of this section show that the detonation speeds measured from both 1D laminar detonation simulations differ from those obtained from ZND theory by less than 0.5%.

B. From 1D laminar to 2D cellular and 2D transverse detonations

A 1D detonation in an AB sample with a transverse cross section of 8.1 nm × 7.8 nm becomes unstable with an increase of the reaction barrier from 0.198 to 0.245 eV, resulting in complete collapse of the detonation wave after ~20 ps. The source of this collapse is the increased sensitivity of the chemical reactions to pressure changes upon increase of steepness in the $P(V)$ Hugoniot of reactants that results in a substantial decrease in the reaction zone thickness. The length scale of spontaneous longitudinal perturbations and fluctuations in pressure and temperature then becomes comparable to the thickness of the reaction zone, which may cause a decrease in pressure to below that within the von Neumann spike where reactions are initiated. Such change, coupled with the decrease in the chemical reaction rate, results in longitudinal instability of the detonation front that leads to the decay of detonation with time.

The collapse of the 1D detonation does not happen if PBCs are applied over a somewhat larger distance in one of the transverse directions. Indeed, once one of the transverse dimensions of the MD box is quadrupled, the 1D detonation wave develops into a stable, but more complex, 2D nonplanar detonation front that insulates the reaction zone against large spontaneous fluctuations in pressure and temperature. In particular, disturbances at the planar detonation front now evolve into a cellular structure, induced by localized "hot" spots within the leading shock front. Such cellular patterns are well known in the gas phase [1,2], where their evolution from a planar shock front due to instabilities has been studied

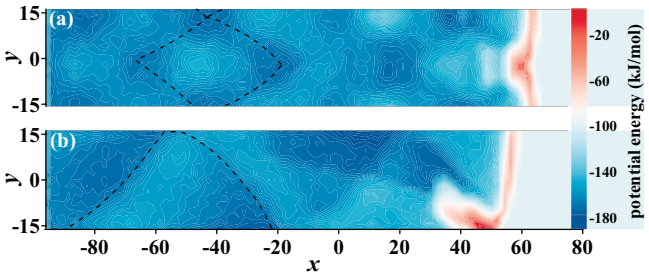

FIG. 7. (Color online) Snapshots of 2D cellular detonations in the AB solid with $L_y = 32.4$ nm, $L_z = 31.2$ nm, and $E_b = 0.367$ eV. Potential energy maps are shown for a simulation employing (a) PBCs in both the y and z transverse directions and (b) RBCs in the y direction and PBCs in z direction. The dashed cell in (a) has the transverse y dimension of the MD box $L_y = 32.4$ nm, while in (b) only half of a cell fits along the same direction. The detonation speed in the x direction in the top pane is 8.344 km/s and in the bottom pane 8.285 km/s.

at the continuum level. [20–22,44] It is remarkable that our minimalist AB model is able to spontaneously generate structures so similar to those studied in detonating gases but at a much smaller scale, presumably because of the far shorter reaction zone length (~1 nm vs ~10 mm).

The pressure in the hot spots is higher than that in the von Neumann spikes observed in the quasistable 1D MD simulations used to start the 2D MD simulations. Figure 7(a) displays the cellular pattern of the detonation front in an AB sample having a reaction barrier $E_b = 0.367$ eV, and employing PBCs in both the y and z transverse directions. In this case, a single cell fits along the y dimension of the MD box, the cellular structure being generated by a single Mach stem and two transverse shock waves moving along the detonation front, all visible in Fig. 7(a). The detonation cell has a transverse y dimension equal to that of the MD box, $L_y = 32.4$, while the cell's x dimension is 45 nm. Employing the same AB sample while using RBCs in the y direction and PBCs in the z direction results in a cellular structure with only half of a cell fitting along the y transverse direction of the same size box. Such a cellular structure is induced by a powerful Mach stem appearing upon collision of the transverse shock wave with the rigid walls [see Fig. 7(b)].

A cellular structure is also observed in samples of larger transverse dimensions. Figure 8(a) displays the cellular detonation structure in an AB solid with $L_y = 105.6$ nm, $L_z = 15.6$ nm, $E_b = 0.367$ eV, and PBCs applied in both the y and z directions. In contrast to the case with $L_y = 32.4$ nm discussed above, two cells induced by two Mach stems, visible in Fig. 8(a), fit into the box in the y direction. Each cell has a length of ~65 nm in the x direction and a height of ~52.6 nm in the y direction. More generally, for such configurations, we have found that PBCs allow an integer number of cells along the y direction, in contrast to RBCs that allow a half-integer number.

As time progresses, the cellular 2D detonation structure depicted in Fig. 8(a) suddenly transforms into a "transverse" 2D detonation consisting of the three-headed detonation wave structure shown in Fig. 8(b). See Supplemental Video S1 [43].

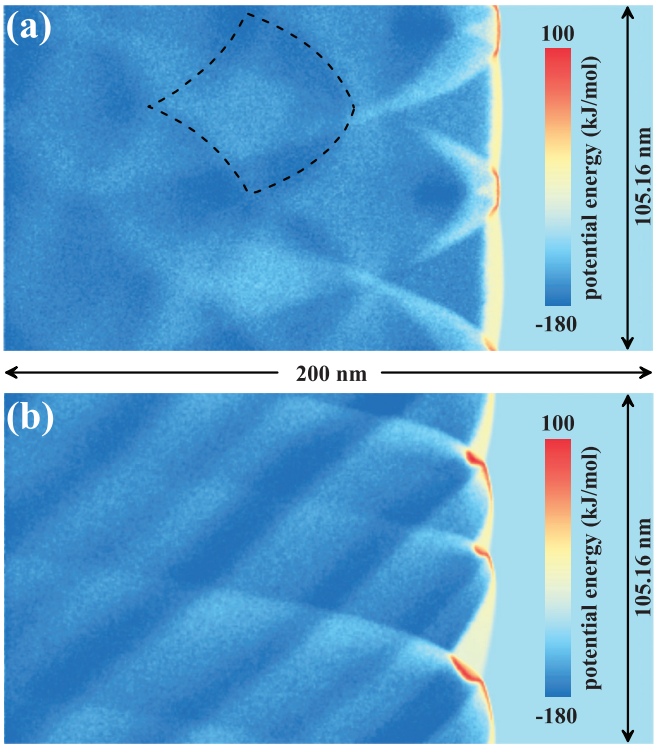

FIG. 8. (Color online) Snapshots of 2D (a) cellular and (b) transverse detonations in an AB solid with $E_b = 0.367$ eV, $L_y = 105.16$ nm, $L_z = 15.6$ nm, and PBCs applied in both y and z transverse directions. The cellular detonation (a) is suddenly transformed into a transverse detonation (b) at time $t \approx 170$ ps. See Supplemental Video S1 [43]. The map of the potential energy in (a) shows a two-headed cellular detonation, where each head is composed of a Mach stem and two transverse shocks. The transverse shocks propagate in opposite directions and collide periodically with each other to form new Mach stems. The map of the potential energy in (b) displays a three-headed transverse detonation (see details in Fig. 9), where the heads are propagating without collisions along the y direction. The dashed cell in (a) has a transverse y dimension equal to half of the MD box $L_y/2 = 52.6$ nm, while its length along x is ~65 nm. Both detonations are propagating with a speed of 8.30 km/s along the x direction. See also Supplemental Videos S1 and S2 [43].

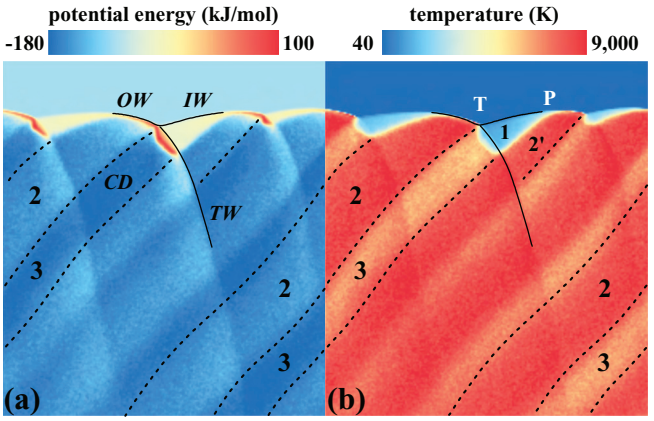

FIG. 9. (Color online) Wave configuration in the 2D three-headed transverse detonation depicted in Fig. 8(b). Both the maps of potential energy (a) and temperature (b) show the incident shock wave (IW), the oblique shock wave (OW), the transverse shock wave (TW), and the contact discontinuity (CD) between "hot" and "cold" flows of products produced by OW and TW. The point T corresponds to an intersection of three shock waves in such a Mach configuration. The weak IW only compresses the incoming reactants but does not ignite them. Reaction zones are then produced by the strong OW and TW. As a result the two types of alternating flow stripes with products at different temperatures appear behind the detonation front. Point P corresponds to transition from OW to IW fronts in adjacent detonation heads.

Each head moves along the detonation front in the transverse y direction and consists of three shock waves: the weak incident shock wave (IW) intersecting with strong oblique (OW) and transverse (TW) shock waves as shown in Fig. 9. These IW, OW, and TW comprise a well-known Mach configuration [45].

The weak IW does not initiate reactions. Rather, the compressed but relatively cold reactants in zone 1 remain intact behind the IW front. The precompressed material in zone 1 is further compressed by the stronger TW front, which initiates chemical reactions resulting in stripe 3 of the products behind the TW front. Because the products are produced by double shock IW and TW compression, they have lower temperature but higher density than those in stripe 2.

In contrast to IW, the OW is strong enough to initiate reactions without additional compression; the incoming reactants are transformed into relatively hot products in a very thin reaction zone right after the OW front, thus forming stripe 2 in Fig. 9. The contact discontinuity (CD) separates stripes 2 and 3, both having the same pressure but differing in other properties.

Although both OW and TW are supported by reaction zones behind the fronts, the weak IW does not have such a reaction zone: very few reactions are induced in 1 by contact with the hot products in stripe 2′. Instead, the contact discontinuity between 1 and 2′ (not shown in Fig. 9) acts as a piston providing pressure support starting from the contact point P between the IW front in a given detonation head and the OW front in the neighboring detonation head.

The three-headed transverse detonation shown in Figs. 8(b) and 9 remains stable, at least for 1 ns (the maximum time allowed in these MW-MD simulations), despite substantial pressure fluctuations in neighboring heads within the leading shock front. In this case, the ~60 nm net thickness of the detonation front is appreciable compared to the 3 nm thickness of the quasistable 1D planar detonation used to start the simulation. The strong oblique waves (also termed Mach waves) and transverse shocks within the detonation heads produce local "hot" spots that are clearly visible in the potential energy maps of Figs. 8(b) and 9 in the detonation front, which have pressure and temperature much higher than those in the von Neumann spike of 1D planar detonation at the beginning of the simulation. The acceleration of the chemical reactions in these localized hot spots stabilizes the 2D transverse detonation structure, making it insensitive to spontaneous pressure fluctuations.

The pure transverse detonation regime cannot ultimately be stable under experimental conditions because the transverse wave would eventually collide with walls and another transverse wave moving in the opposite direction. MD

simulation of an AB solid with $L_y = 105.6$ nm, $L_z = 15.6$ nm, $E_b = 0.367$ eV, and RBCs applied in the y direction shows that such collisions lead to the formation of a cellular-like detonation pattern. See Supplemental Video S2 [43]. However, collisionless regimes, similar to those obtained in this work, were observed in simulations of gas-phase detonation in a channel with PBCs [20]. The only possible way to generate a collisionless detonation pattern in experiment is to initiate the detonation wave in a tube, which might result in the appearance of a spinning detonation. Such a possibility is currently under investigation.

C. 3D multiheaded pulsating detonations

Once the transverse dimensions 8.1 nm × 7.8 nm of the original AB solid sample with reaction barrier 0.367 eV are both increased by a factor of 13, to $L_y = 105$ nm, $L_z = 101$ nm, with PBCs still applied, the 1D detonation, originally propagating with speed 8.4 km/s, is transformed into a multiheaded 3D detonation propagating with almost the same net speed. At the very least, this 3D detonation involves many modes displaying no easily discernible pattern. Such phenomena have also been observed experimentally in gases [1,2] and diluted liquid explosives [16,26,27], and were termed pulsating-turbulent detonations.

Transition from 1D detonation to this nominally turbulent regime begins with the development of small ripples in the planar front that appear within the first several picoseconds. Then, the ripples grow into a nonplanar 3D structure consisting of alternating hot and cold zones resulting in a net increase in the detonation front thickness from 3 nm to ~40 nm. This multiheaded 3D detonation is characterized by a highly inhomogeneous distribution of pressure in the interval 21–70 GPa. Figure 10 shows maps of the potential energy and fraction $\lambda(A_2, B_2)$ of reaction products within the transverse $y \times z$ cross section of the detonation front. The dark blue spots in the right panel correspond to low-pressure regions ~21 GPa, while the bright red spots correspond to high-pressure regions up to 70 GPa, which is much higher than 52 GPa in vN spike achieved in the starting 1D detonation.

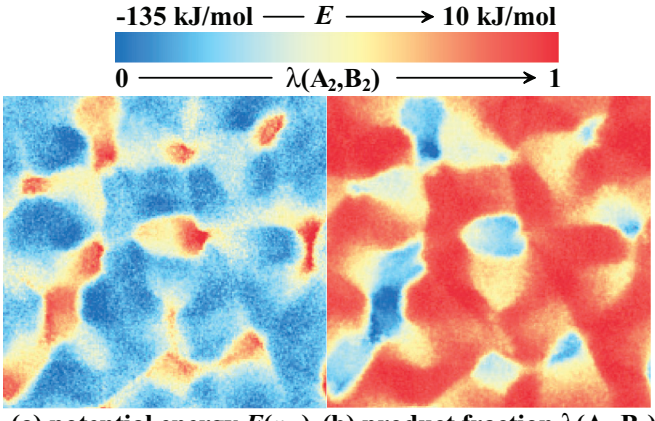

FIG. 10. (Color online) Snapshots of the 3D multiheaded pulsating detonation structure at the shock front in an AB solid with $L_y = 105$ nm, $L_z = 101$ nm, $E_b = 0.367$ eV, and PBCs in the transverse directions. The left panel provides a map of the potential energy in the transverse yz cross section. The right panel provides the corresponding map of the fraction $\lambda(A_2, B_2)$ of reaction products. Also see Supplemental Video S3 [43].

Although the multiheaded 3D detonation persists within the time scale of the MW-MD simulation (up to 100 ps), its local dynamics involve the appearance and disappearance of many low-pressure and high-pressure spots. Within the detonation front there are many high-pressure detonation heads where chemical reactions are ignited, thus forming hot spots. In contrast to the traditional picture of hot spots, which plays an important role in detonation initiation in EMs, and which require the presence of preexisting defects [46], the observed hot spots appear as detonation heads within the irregular structure of the detonation front without such defects.

VI. SUMMARY AND CONCLUSIONS

We were able to simulate a series of complex detonation structures by combining an AB model with the MW-MD technique. Which structure is observed depends on the physico-chemical properties of the AB solid as represented by the reaction barrier E_b, the geometry of the sample, and the boundary conditions. Quasi-1D samples with $L_x = 200$ nm, $L_y = 8.1$ nm, and $L_z = 7.8$ nm, and PBCs applied in y and z directions, sustain stable planar detonation waves propagating along the x direction in AB material with $E_b < 0.2$ eV. In those cases the detonation speeds obtained in MW-MD simulations are in excellent agreement with predictions of continuum ZND theory. However, for AB samples of the same geometry but higher reaction barriers, $E_b = 0.245$ and 0.367 eV, the 1D detonation decays with time due to the development of longitudinal perturbations. This collapsing 1D detonation is stabilized by transverse perturbations leading to a stable 2D cellular detonation upon increase of just one transverse dimension of the simulation box by a factor of 4. The same cellular detonation pattern persists if another transverse dimension is also increased by a factor of 4, giving a cross section of 32.4 nm × 31.2 nm.

The type of boundary conditions affects the geometry of the cellular patterns: detonation cell size in the y direction doubles if the PBC along the y direction is replaced by a RBC. Moreover, PBCs were observed to lead to an integer number of cells in the largest transverse direction, while a RBC in that direction produces half-integer number of cells.

A stable cellular pattern is observed to become destabilized and eventually transforms into a stable 2D transverse detonation upon increase of the reaction barrier E_b from 0.245 to 0.367 eV in the sample with PBCs in the transverse dimensions and a 105.16 nm by 15.6 nm cross section. However, for the same $E_b = 0.375$ eV and boundary conditions, increase of the sample cross section to $L_y = 105$ nm and $L_z = 101$ nm, leads to a stable 3D multiheaded pulsating detonation.

Single or multiple detonation heads are the general features of the complex detonation front structures observed in our simulations. These heads are composed of localized regions of high density and pressure, substantially exceeding those in the von Neumann spike predicted by 1D ZND theory. Such dynamical high-pressure zones serve as hot spots where

combustion is initiated during detonation propagation even in defect-free samples. These highly localized, spontaneously arising regions stabilize the non planar detonation fronts, making them insensitive to pressure and temperature perturbations. The instabilities and associated detonation regimes found in the condensed phase AB energetic material closely parallel detonation behavior in the gas phase. Such remarkable resemblance suggests a universal nature for planar detonation front instabilities inherent to both condensed and gas-phase detonations.

ACKNOWLEDGMENTS

The work at USF and NRL was supported by the Naval Research Laboratory and the Office of Naval Research. The work at USF was also supported by the National Science Foundation (NSF) and the Defense Threat Reduction Agency. Simulations were performed using the NSF Extreme Science and Engineering Discovery Environment (XSEDE) facilities, the USF Research Computing Cluster, and the computational facilities of the Materials Simulation Laboratory at USF.

[1] W. Fickett and W. C. Davis, *Detonation* (University of California Press, Berkeley, 1979).
[2] J. H. S. Lee, *The Detonation Phenomenon* (Cambridge University Press, Cambridge, 2008).
[3] D. L. Chapman, Philos. Mag. **47**, 90 (1899).
[4] E. Jouguet, J. Math. Pures Appl. **1**, 347 (1905).
[5] E. Jouguet, J. Math. Pures Appl. **2**, 5 (1906).
[6] Ya. B. Zeldovich, Zh. Eksp. Teor. Fiz. **10**, 542 (1940).
[7] J. von Neumann, in *John von Neumann, Collected Works*, edited by A. J. Taub, Vol. 6 (Macmillan, New York, 1963).
[8] W. Doering, Ann. Phys. **435**, 421 (1943).
[9] Y. B. Zel'dovich and A. Kompaneets, *Theory of Detonation* (New York, Academic, 1960).
[10] R. E. Duff and H. T. Knight, J. Chem. Phys. **20**, 1493 (1952).
[11] B. Voitsekhovskii, V. Mitrofanov, and M. Y. Topchiyan, Wright Patterson AFB Rept. FTD-MT-64-527, AD-633,821 (1966).
[12] B. Voitsekhovskii, V. Mitrofanov, and M. Topchiyan, Combust. Explos. Shock Waves **5**, 267 (1969).
[13] G. L. Schott, Phys. Fluids **8**, 850 (1965).
[14] K. I. Shchelkin, Physics-Uspekhi **8**, 780 (1966).
[15] F. Zhang and H. Gronig, Phys. Fluids A **3**, 1983 (1991).
[16] D. Matsukov, V. Solovev, and S. Sorokin, Combust. Explos. Shock Waves **30**, 563 (1995).
[17] J. A. Fay, Physics Fluids **2**, 283 (1959).
[18] J. J. Erpenbeck, Phys. Fluids **13**, 2007 (1970).
[19] H. I. Lee and D. S. Stewart, J. Fluid Mech. **216**, 103 (1990).
[20] A. Bourlioux and A. J. Majda, Phil. Trans. R. Soc. A **350**, 29 (1995).
[21] M. Short and D. S. Stewart, J. Fluid Mech. **368**, 229 (1998).
[22] V. Deledicque and M. V. Papalexandris, Combust. Flame **144**, 821 (2006).
[23] N. Tsuboi, K. Eto, and A. Hayashi, Combust. Flame **149**, 144 (2007).
[24] B. D. Taylor, A. R. Kasimov, and D. S. Stewart, Combust. Theor. Model. **13**, 973 (2009).
[25] J. Shepherd, Proc. Combust. Inst. **32**, 83 (2009).
[26] A. N. Dremin and O. K. Rosanov, Dokl. Akad. Nauk SSSR **139**, 137 (1961).
[27] H. D. Mallory, J. Appl. Phys. **47**, 152 (1976).
[28] D. W. Brenner, M. L. Elert, and C. T. White, in *Shock Compression of Condensed Matter–1989*, edited by S. C. Schmidt, J. N. Johnson, and L. W. Davison (Elsevier Science Publishers, Amsterdam, 1990), p. 263.
[29] C. T. White, D. H. Robertson, M. L. Elert, and D. W. Brenner, in *Microscopic Simulations of Complex Hydrodynamic Phenomena*, edited by M. Mareschal and B. L. Holian (Plenum Press, New York, 1992), pp. 111–123.
[30] D. W. Brenner, D. H. Robertson, M. L. Elert, and C. T. White, Phys. Rev. Lett. **70**, 2174 (1993).
[31] For a review, see C. T. White, D. R. Swanson, and D. H. Robertson, *Chemical Dynamics in Extreme Environments*, edited by R. Dressier (World Scientific, Singapore, 2001), Chap. 11, pp. 547–592.
[32] G. M. Barrow, in *Physical Chemistry*, 5th ed. (McGraw-Hill, New York, 1988), p. 836.
[33] B. M. Rice, W. Mattson, J. Grosh, and S. F. Trevino, Phys. Rev. E **53**, 623 (1996).
[34] A. J. Heim, N. Grønbech-Jensen, E. M. Kober, and T. C. Germann, Phys. Rev. E **78**, 046710 (2008).
[35] V. V. Zhakhovskii, K. Nishihara, and S. I. Anisimov, JETP Lett. **66**, 99 (1997).
[36] V. V. Zhakhovsky, M. M. Budzevich, N. A. Inogamov, I. I. Oleynik, and C. T. White, Phys. Rev. Lett. **107**, 135502 (2011).
[37] M. M. Budzevich, V. V. Zhakhovsky, C. T. White, and I. I. Oleynik, Phys. Rev. Lett. **109**, 125505 (2012).
[38] V. V. Zhakhovskii, S. V. Zybin, K. Nishihara, and S. I. Anisimov, Phys. Rev. Lett. **83**, 1175 (1999).
[39] A. J. Heim, N. Grønbech-Jensen, E. M. Kober, J. J. Erpenbeck, and T. C. Germann, Phys. Rev. E **78**, 046709 (2008).
[40] S. I. Anisimov, V. V. Zhakhovskii, and V. E. Fortov, JETP Lett. **65**, 755 (1997).
[41] H. M. Mott-Smith, Phys. Rev. **82**, 885 (1951).
[42] B. L. Holian, M. Mareschal, and R. Ravelo, J. Phys. Chem. **133**, 114502 (2010).
[43] See Supplemental Material at http://link.aps.org/supplemental/10.1103/PhysRevE.90.033312 for videos S1–S3.
[44] V. N. Gamezo, D. Desbordes, and E. S. Oran, Combustion Flame **116**, 154 (1999).
[45] R. Courant and K. O. Friedrichs, *Supersonic Flow and Shock Waves* (Interscience Publishers, New York, 1948).
[46] J. E. Field, N. K. Bourne, S. J. P. Palmer, S. M. Walley, J. Sharma, and B. C. Beard, Phil. Trans. Roy. Soc. A **339**, 269 (1992).